Zn-Based Catalysts for Selective and Stable Electrochemical CO_2 Reduction at High Current Densities

Ilias Stamatelos,[1, 2] Cao-Thang Dinh,[3, *] Werner Lehnert,[1, 2] Meital Shviro[1, *, #]

[1] Forschungszentrum Jülich GmbH, Institute of Energy and Climate Research, Electrochemical Process Engineering (IEK-14), 52425 Jülich, Germany

[2] Faculty of Mechanical Engineering, RWTH Aachen University, 52056 Aachen, Germany

[3] Department of Chemical Engineering, Queen's University, Kingston, Ontario, K7L 3N6, Canada

[#] Present address: Chemistry and Nanoscience Center, National Renewable Energy Laboratory (NREL), Golden, CO, 80401, United States

*To whom correspondence should be addressed

meital.shviro@nrel.gov; caothang.dinh@queensu.ca

Abstract

Practical electrochemical carbon dioxide (CO_2) reduction requires the development of selective and stable catalysts based on low-cost and Earth-abundant materials. In this work, we develop catalysts for CO_2 conversion to CO based on ZnO with various morphologies, including nanoparticles, nanorods, nanosheets, and random shapes. We found that ZnO nanorods exhibit the highest CO_2 to CO efficiency, with a high CO Faradaic efficiency (FE) of over 80% in a current density range of 50-160 mA cm^2 in both flow-cell and membrane electrode assembly (MEA) reactors. We found that the CO selectivity of ZnO-based catalysts slowly decreased over time at high current densities due to depletion of the ZnO phase. We have developed an *in-situ* regeneration strategy for catalysts that involves periodic oxidations of the catalysts during electrochemical CO_2 reduction. Using this approach, we have demonstrated the conversion of CO_2 to CO with a stable CO FE above 80% for 100 hours at a current density of 160 mA cm^{-2}.

Keywords: Zinc Oxide, nanomaterials, membrane-electrode-assembly, electrochemical CO_2 reduction, *in-situ* regeneration, CO_2-to-CO.

Introduction

The electrochemical carbon dioxide (CO_2) reduction reaction (ECR), powered by renewable energy sources, such as wind and solar, offers a compelling route for the use of CO_2 as a sustainable feedstock for the production of fuels and chemicals. [1–3] Significant advances in the fundamental understanding of ECR [4–6] and demonstration of its potential application have been achieved in the last decade. [7] Recent techno-economic studies have highlighted the importance of achieving high current densities

(i.e., hundreds of mA cm^{-2}) for the ECR to be economically feasible. [8–11] Moreover, the catalyst is responsible for a major part of the total ECR overpotential [12], dictating the importance of developing an efficient cathode Gas Diffusion Electrodes (GDE) for ECR. The catalyst efficiency should be evaluated in equal terms of performance and stability since the latter introduces a significant techno-economical aspect for ECR application. [13]

The ECR can produce a variety of products, depending on the type of catalyst used. [14,15] Among the possible products, CO and $HCOO^-$ are the simplest and have a high potential economic value compared with other products. [16, 10] In particular, CO appears to be a promising product because it can be used as a valuable industrial intermediate to produce other chemicals, such as methanol and synthetic fuels. [17, 18] Several electrocatalysts are known to have high efficiency in the formation of CO. However, they are mainly based on expensive noble metals such as Au, Ag, and Pd. [19–21]

Among non-noble metal catalysts, Zinc (Zn) has been demonstrated as an effective catalyst for CO_2 reduction to CO. Many studies have been focusing on improving the efficiency of Zn-based catalysts by altering its morphology [22–24], controlling its oxidation state [25] or doping. [26] Luo et.al. [27] demonstrated a high-performance Zn-cathode by creating an active Zn-foam, exploiting its high surface-area. The oxide-derived Zn (OD-Zn) emerged as a catalytically active material, owning to its increased active surface area and grain-boundaries concentration. [28, 29] Apart from its pristine metallic form, Zn exhibited remarkable ECR performance in sulphide [30] (ZnS_2) and oxide [31] (ZnO) structures. The latter has attracted further interest not only for its ECR performance but also for its ability to act as an active catalyst substrate for various (catalytically active) d-block metals. [32]

While much research has been devoted to improving the performance of such Zn-based catalysts, most of these studies performed ECR in aqueous (H-cell) systems where the current densities are limited to below 50 mA cm^{-2}. [23] Recently, ZnO has been also employed as an electrocatalyst for the CO_2-to-CO conversion [33] exhibiting promising ECR performance, owing to its crystalline structure and nature of active sites. [30] Further information on the ZnO activity was provided by the work of Zong et.al. [35], identifying the oxygen-vacancies, in the ZnO structure, to be responsible for enhancing the ECR activity of this material. Nonetheless, only a handful of works demonstrated the performance of ZnO catalysts at industrially relevant current densities (>150 mA cm^{-2}) [36, 27,35], while omitting any reference to catalyst stability at high current densities. Previous works on Zn-based catalysts suggested that these materials exhibit limited stability for current density above 80 mA cm^{-2}. [27]

In this work, we developed selective and stable ZnO-based catalysts for CO_2 reduction to CO. ZnO nanoparticles were synthesized with different morphologies, including nanorods (NR), nanosheets (NS), nanoparticles (NP), and random shapes (RS).The performance of ZnO catalysts was evaluated using both flow-cell and membrane electrode assembly (MEA) electrolyzers which allow high current density operation. We found that ZnO NR shows high CO Faradaic efficiency of over 80% at a current density higher than 160 mA cm^{-2} in both cell configurations. In the MEA cell, the ZnO NR maintained high CO selectivity for 10 hours before it began to decrease due to ZnO

phase depletion. To extend the operation time, we developed an *in-situ* catalyst regeneration in which the ZnO oxide phase was regenerated periodically. Using this approach, we demonstrated ZnO catalysts that maintained a high CO FE of over 80% for more than 100 hours at 160 mA cm^{-2} in the MEA cell.

Experimental Section

Materials and Chemicals

Chemical and materials: zinc nitrate hexahydrate ($Zn(NO_3)_2 \cdot 6H_2O$, 99.99%), potassium hydroxide (KOH, 99%), zinc acetate ($Zn(OCH_3)_2$, 99.99%), ethanol (anhydrous), sodium perchlorate ($NaClO_4$, 99.999%) were purchased from Sigma-Aldrich and used without further purification. Urea (CH_4N_2O, 99.99%), Iridium/Iridium (III) Oxide nano-powder (IrO_x, nanopowder 99.99%), silver nanopowder (99.99%, 20-40 nm) were purchased from Alfa-Aesar and used without any purification. Demineralised (MiliQ) water. Carbon Paper (Sigracet B22), titanium fibres porous transport layer (Ti-PTL, 500 μm thickness), Nafion (5 % wt/wt, alcohol based), Ni-foam (500 μm thickness) and Carbon Black (Cabot Vulcan XC-72) were purchased from Fuel-Cell Store. Sustainion Membrane (X37-50 grade RT) was purchased from Dioxide Materials.

Synthesis of the catalysts

ZnO catalyst with different particle morphologies were synthesised using wet-chemical techniques.

ZnO nanoparticles (NP). A 50 ml solution of 0.2 M $Zn(NO_3)_2$ (99.99%) was prepared. To that solution, 50 ml of 0.4 M KOH was added dropwise, under a stirring condition until the end of the process. The precipitant was collected via centrifugation and washed 3 times with water (MilliQ) and 1 time with ethanol. The obtained product was dried overnight (70 ^oC) and calcined for 3 h at 500 ^oC, to form the crystalline phase of ZnO. The ZnO with random shape (RS) was prepared using a similar procedure except the addition of 50 ml of 1 M KOH instead of 0.4 M KOH. [66]

ZnO nanosheets (NS). Typically, 50 ml of 0.2 M zinc acetate ($Zn(OCH_3)_2$, 99.99% Sigma-Aldrich) were added dropwise in a 50 ml solution of 0.4 M urea (CH_4N_2O). The mixture was then refluxed at 90 ^oC for 2 h. The precipitant was washed collected and washed 3 times with water and 1 time with ethanol. The obtained product was dried overnight (70 ^oC) and afterwards calcined for 2 h at 400 ^oC, to form the crystalline phase of ZnO in the nanosheet morphology. [37]

ZnO nanorods (NR). In a typical synthesis, 0.89 g of $Zn(NO_3)$ and 0.54 g of urea (CH_4N_2O) were dissolved in 100 ml mixture of water and ethanol (80 ml/20 ml). To this mixture, 0.1 M of HNO_3 was added, until the pH was adjusted among 2.0-3.0. The resulting solution was boiled and refluxed for 8 h in a round-bottom flask. The resulting precipitant was collected and washed 3 times with water and 1 time with ethanol. The powder was dried overnight (70 ^oC). High temperature calcination is not needed since the allotrope powder is already crystalline. [67]

Electrode fabrication

Gas diffusion electrodes (GDEs) were prepared on a Sigracet (22B) carbon paper with microporous layer using an automatic spray coating machine (Sono-Tek, ExactaCoat). The ink was composed of 120 mg of catalyst powder, 30 mg of carbon black, 12 ml of isopropanol, 7.5 ml of water (Milli-Q), and 158.3 µl of Nafion solution (5% wt/wt). The ink was put under Ultra-Turex (33.000 rpm) for 5 min and following into a sonication bath for 60 min. The same ink recipe (content of solids and solvents ratio) was used also for the preparation of the Ag-GDE. The Ag-GDEs were fabricated using commercial Ag nano-powder and loading of 1 mg cm^{-2}. After preparation, all the different GDEs prepared were dried at 70 ^{o}C for 3 h. This heat treatment aims to evaporate the residual surfactants from the ionomer suspension and the dispersive media.

For the MEA anode, a Ti fibre-mesh was used as the PTL (porous transport layer). The original Ti-PTL was etched in concentrated boiling HCl (1 M), in order to break-down the initial passivating TiO_x layer. The etched PTL was sprayed with IrO_x nanoparticles (Alfa-Aesar) to form the anode catalyst layer. The ink composition used for the anode was: 40 mg of IrO_x and 10 mg of Nafion Ionomer (in ethanolic 5% w/w solution) were dispersed in 5 ml methanol. The loading of IrO_x was 2mg cm^{-2}.

Electrochemical measurements

Electrochemical experiments were performed in a flow-cell (Electro-Cell) with an active area of 1 cm^2. The reference electrode was Ag/AgCl and the applied potentials were related with an RHE using the equation: $E_{RHE} = E_{Ag/AgCl} + 0.059PH + 0.1976$. The electrolyte used was 1 M KOH with a flow rate of 4.6 ml min^{-1}, while the CO_2 was fluxed at 16 sccm. The electrochemical performance was evaluated from the polarization curve of the material in the potential window of -0.4 V to -1.2 V (vs RHE). In the flow cell, the counter electrode was Ni-foam. For each point of the polarization curve, the GDE was potentiostatically run for 25 min.

Electro-Chemical-Surface-Area (ECSA) was estimated in an H-cell with 0.1 M $NaClO_4$ (Ar saturated) as electrolyte, using an Ag/AgCl reference electrode and a Pt wire as a counter electrode and the ECR catalysts deposited over the carbon paper. This electrolyte was used in order to minimize any ion characteristic adsorption and be able to eliminate the effect of the carbon paper (substrate). [68]. The ECSA was measured after the catalyst-layer activation, with scan rates among 7.5-100 mV sec^{-1}. the measure of the ECSA was estimated through the double-layer capacitance (Cdl), since the nature of the catalyst and the consistency of the GDE remained the same. The survey CVs were obtained from -0.2 to 0.2 V (vs Ag/AgCl), while the potential window selected for the Cdl calculation was –0.1 to 0.1 V (vs Ag/AgCl). For the Tafel-Slopes and the Potentiostatic-Impedance-Spectroscopy (PEIS), the electrolyte used was 1 M KOH, and were measured in the Flow-Cell set-up at a low current range of 5 - 18mA cm^{-2}. To achieve high accuracy for CO product analysis during the Tafel-Slopes analysis, we used low flow-rate of CO_2 reactant (18 sccm). The PEIS was measured at the onset-potential of each catalyst. All electrochemical experiments were controlled through an AUTOLAB potentiostat coupled with Nova software.

For the measurements of CO_2 reduction in MEA configuration, a customized cell with an active area of 2 cm^2 (1x2 cm^2) The anode was IrO_x/Ti-PTL while the anolyte was 0.1 M $KHCO_3$. Sustainion AEM (X37-50 RT) membrane with a thickness of ~ 50 microns was used. The CO_2 (30 sccm) was humidified at room temperature before entering the cell. The PTFE gasket used, had 400 μm thickness and the cell was assembled by applying 2 Nm torque. The cathode materials were our ZnO-based catalysts and the commercial Ag-NP for as comparison media. The catalyst layer of the anode and the cathode were facing the AEM membrane during the assembly of the cell. The polarization curve was produced by leaving the cell running for 25 min at fixed current. During this time the average necessary voltage to maintain this current was assed and the products were collected after 20 minutes.

For both flow-cell and MEA reactor, the CO_2 reduction products were analysed using an in-line gas chromatography (PerkinElmer) coupled with a thermal conductivity detector (TCD) and a flame ionization detector (FID). Argon gas (99.999%) was used as carrier gas.

Characterisation

The crystalline phase of the pristine ZnO and the prepared GDEs were characterized by X-ray diffraction (XRD) using CuKα radiation in the 2θ range from 25 to 100 °, employing a Shimadzu XRD-6000 diffractometer.

The surface compositions of the prepared catalysts were analysed using X-ray photo-electron spectroscopy (XPS) (Phi5000 VersaProbeII, ULVAC-Phi Inc., USA). The radiation source was Al K-alpha, monochromatic (1.486 keV) with X-ray setting: 50W, 15kV, 200μm spot. The survey spectra were obtained applying 187.5 eV pass energy, 0.8 eV step, 100 ms/step and the detailed spectra by applying 23.5 eV pass energy, 0.1 eV step, 100 ms/step.

The morphology of the catalyst powders and the GDEs was observed with scanning electron microscope (SEM). For this purpose, the Zeiss 1550 VP Scanning Electron Microscope was used with a Gemini column, up to 30keV.

The inherent hydrophobicity of the catalyst layer was assessed with Kruss DSA25 Drop Shape Analyzer. For the measurement 10 μl of MilliQ water were dropped on the catalyst layer. The measurement of the contact angle was done under static conditions (Cassie-Baxter).

Results and discussion

Catalyst synthesis and Characterisations

Scanning electron microscopy (SEM) was used to investigate the morphologies of the prepared catalysts (Figure 1A-D) and confirm the successful synthesis of ZnO allotropes with different morphologies. The wet-chemical synthetic approach leads to the formation of ZnO with morphologies of nanoparticles (NP, Figure 1A), random-shape (RS, Figure 1B), nanosheets (NS, Figure 1C), and nanorods (NR, Figure 1D). The NR exhibits a small diameter (80 nm) and a large aspect ratio (20:1, length: diameter), and the NS exhibits an average thickness of 20 nm. The NP exhibits small

diameter (of 20 nm), while the RS is formed in larger agglomerates (Figure S1). The X-ray diffraction results (XRD, Figure 1 E) reveal a well-defined crystallographic pattern that can be indexed to ZnO hexagonal wurtzite structure (JCPDS #75-576), without impurities, for all samples. As observed in Figure 1E, the XRD pattern of NS exhibits broader peaks compared to those of other allotropes. This characteristic is attributed to the 2D morphology of the NSs, as explained also by Scherer's equation and observed in other studies. [37, 38, 39]

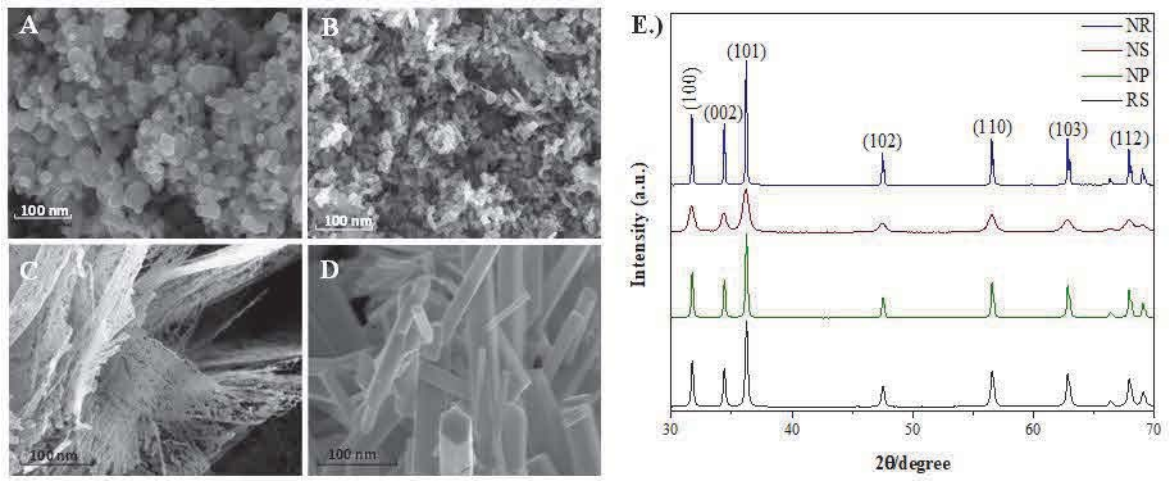

Figure 1: SEM and XRD characterisation of the synthesised ZnO-based catalyst materials. A.) SEM image of ZnO-NP, B.) SEM image of ZnO-RS, C.) SEM image of ZnO-NS, D.) SEM image of ZnO-NR, E.) XRD diffractogram of all the ZnO powders with different morphology.

X-ray photoelectron spectroscopy (XPS) was used to study the chemical state of the ZnO catalysts at the surface (Figure 2). All survey XPS spectra (Figure 2A) show characteristic peaks in the binding energy range of 1200-100 eV, confirming the presence of Zn and O and the absence of impurities. Additional peaks (KLMM, K2s, K2p) observed in the spectrum of ZnO NP, are due to the presence of potassium left-over from the synthesis. Quantification of the elemental composition reveals differences in the amount of Zn and O atoms on the surface of each allotrope (Figure 2A). The ZnO NR presents the highest ratio of Zn:O (1.24:1), while the Zn:O ratio in the NS is calculates at 1.2:1. These two allotropes exhibit the highest percentage of Zn-atoms on their surface in comparison with the rest of the materials. The difference at the surface ratio of Zn:O can be attributed the lattice vacancies, O-defects and O-vacancies, different for each allotrope material. [40,41] Therefore, it can be concluded that the ZnO-NR presents more O-vacancies than the other ZnO-based catalysts. [35] The high-resolution spectra (Figure 2B) for Zn (Zn2p3) also show differences in the binding energies of the characteristic Zn peaks. A difference of 0.7 eV in the position of the Zn-peaks can be observed among our materials, which can be attributed to the distinct difference in morphology, crystallinity, and oxygen-vacancies in the materials' lattice, as observed in previous studies. [24,35,42–44] The high-resolution O1s XPS spectra of all allotropes show two deconvoluted peaks at 530 eV and 531.6 eV, which are attributed to the lattice oxygen and oxygen in the form of surface hydroxy (OH), respectively.

The deconvolution of the O-1s peaks, reveals different ratio between lattice oxygen and surface –OH. From the high-resolution spectra (Figure S2) the ZnO NR presents the highest amount of lattice-oxygen, revealing a clear crystalline structure of the surface.

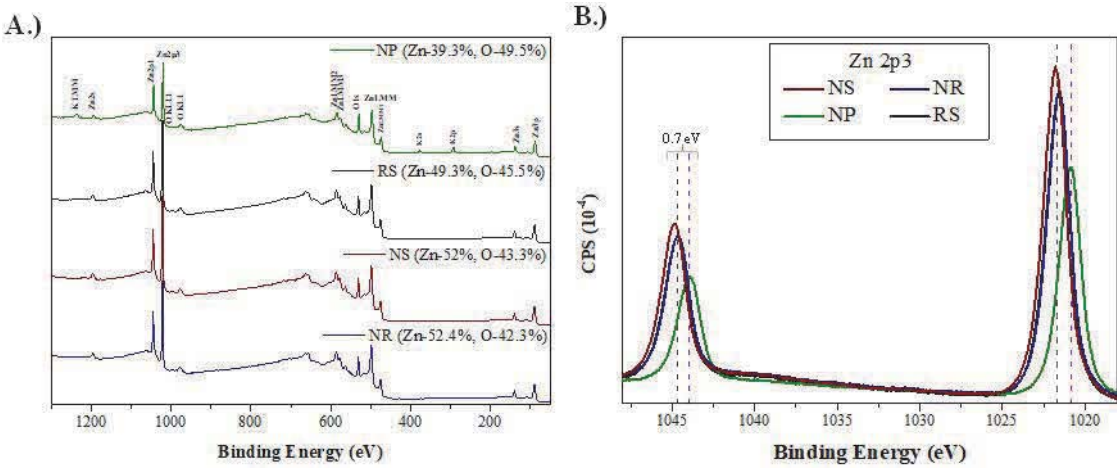

Figure 2: XPS characterisation of the catalyst powders' surface A.) Survey spectra of all the ZnO-based materials, B.) High-Resolution spectra for Zn2p3 of all the ZnO-based materials.

ECR performance in Flow-Cell

To evaluate the catalytic performance of ZnO with different morphologies, we first used a flow cell reactor and an alkaline catholyte and anolyte. Carbon monoxide (CO) Faradaic efficiency (FE_{CO}) and partial current density (J_{CO}) were measured in the potential range of –0.4 to –1.2 V vs. RHE. For comparison, the performance of commercial silver nanoparticles (Ag NPs), which have been demonstrated as excellent catalysts for CO_2 reduction to CO, was also evaluated in similar testing conditions.

All ZnO samples show good CO selectivity at applied potential range of -0.4 to -0.8 V vs RHE, exhibiting FE_{CO} of around 80% (Figure 3A). At more negative applied potentials of -1 and -1.2 V vs RHE, the Zn NR and NS show the highest FE_{CO} of 90 %, which are comparable to the performance of Ag NPs. Interestingly, ZnO NR shows the highest J_{CO} among all allotropes and at all tested applied potentials (Figure 3B). At an applied potential of -1.2 V, ZnO NR exhibits a J_{CO} of -150mA cm^{-2}, while maintaining a good FE_{CO} of 83%, which is a most promising result compared to the performance recorded for ZnO based GDEs (Table S1). To further compare the intrinsic activity of ZnO allotropes, we measured the Tafel-Slopes for the three best ZnO morphologies (NR, NP, and NS). For these measurements, the dependence of J_{CO} on the potentials were studied at very low applied potential range of –0.4 to -0.6 V vs. RHE to avoid the effect of mass transport. We observed similar Tafel-Slope values for the three allotropes, indicating similar reaction kinetics (Figure 3C). However, ZnO NR shows the highest current exchange density of 8mA cm^{-2}, implying its highest intrinsic activity and lower onset potential among the allotropes for the ECR. [45]

To understand the effect of the morphologies on ECR performance of ZnO allotropes, we measured the electrochemical surface area (ECSA) of the samples, after GDE

activation. Among the allotropes, the NR exhibits the highest value of C_{dl} and hence ECSA (Figure 3D). The ECSA characterisation for other allotropes follows the performance-trend observed in the polarization curves (Figure 3B): samples with the higher ECSA exhibit higher $J_{CO.}$

We performed Potentiostatic Impedance Spectroscopy (PEIS) measurement to study the charge transfer resistance (R_{ct}) induced by different ZnO allotropes (Figure S3). The ZnO-nanorod present the lowest R_{ct} and overall resistivity towards the ECR, indicating a more favourable mass-transfer kinetics over the GDE, and a higher ECR activity of this allotrope. This result can be associated with the more active sites available on the nanorods, in an agreement with the tendency exhibited by the rest of the electrochemical characterisations.

For ECR in the gas phase, GDE hydrophobicity can affect CO_2 and water transport and thus catalytic performance. The hydrophobicity of GDE from different ZnO allotropes was characterized by measuring the contact angles (Figure S4). The nanorod GDE exhibits a sharp increase in its inherent hydrophobicity and shows the most significant contact angles compared to the other ZnO GDEs. This property can be attributed to the different ionomer distribution in the allotropes due to the different ECSA of each GDE. Furthermore, this behaviour can also be related to the different morphology itself, as this is a feature that alone can affect the wettability under static conditions. [46,47] Increased hydrophobicity in the catalyst layer has been shown to increase the ECR in flow cell systems by balancing the gas/liquid microenvironment in the catalyst layer. [48]

The physical and chemical changes of the ZnO catalyst during ECR were characterized after the ECR reaction at -160 mA cm^{-2}, for 10 hours. The post-mortem XRD spectra of ZnO NR after continuous operation show a much lower intensity of ZnO peaks compared to pristine ZnO (Figure S5). Additional peaks attributed to metallic-Zn and $Zn(OH)_2$ are observed indicating the reduction of ZnO to metallic Zn during ECR. The presence of $Zn(OH)_2$ could be attributed to the oxidation of metallic Zn to the electrolyte (KOH) after the reaction. The morphology of the ZnO allotropes changed significantly after the ECR reaction (Figure S6 A-C). This is attributed to simultaneous reduction of ZnO to Zn during the ECR reaction, resulting in of the change in morphology. [49] The changes observed in the morphology directly affected the measured hydrophobicity of the GDEs after the ECR conditions (Figure S6E). The ZnO- NR GDE still exhibits the highest contact angle (and thus the highest hydrophobicity), although it decreased compared to its original value. The NP - and NS -ZnO-GDEs exhibit even lower contact angle values after ECR. The NP - and NS -ZnO-GDEs exhibit even lower contact angle values after ECR. The conversion of the oxide phase to a metallic phase is a non-Faradaic process that has been shown to be responsible for the change in catalyst surface area. [50,51]. Although the catalyst morphology changes during ECR, the ZnO- NR catalyst undergoes changes that tend to maintain a uniform catalyst layer that retains its hydrophobic properties to some extent (Figure S6E).

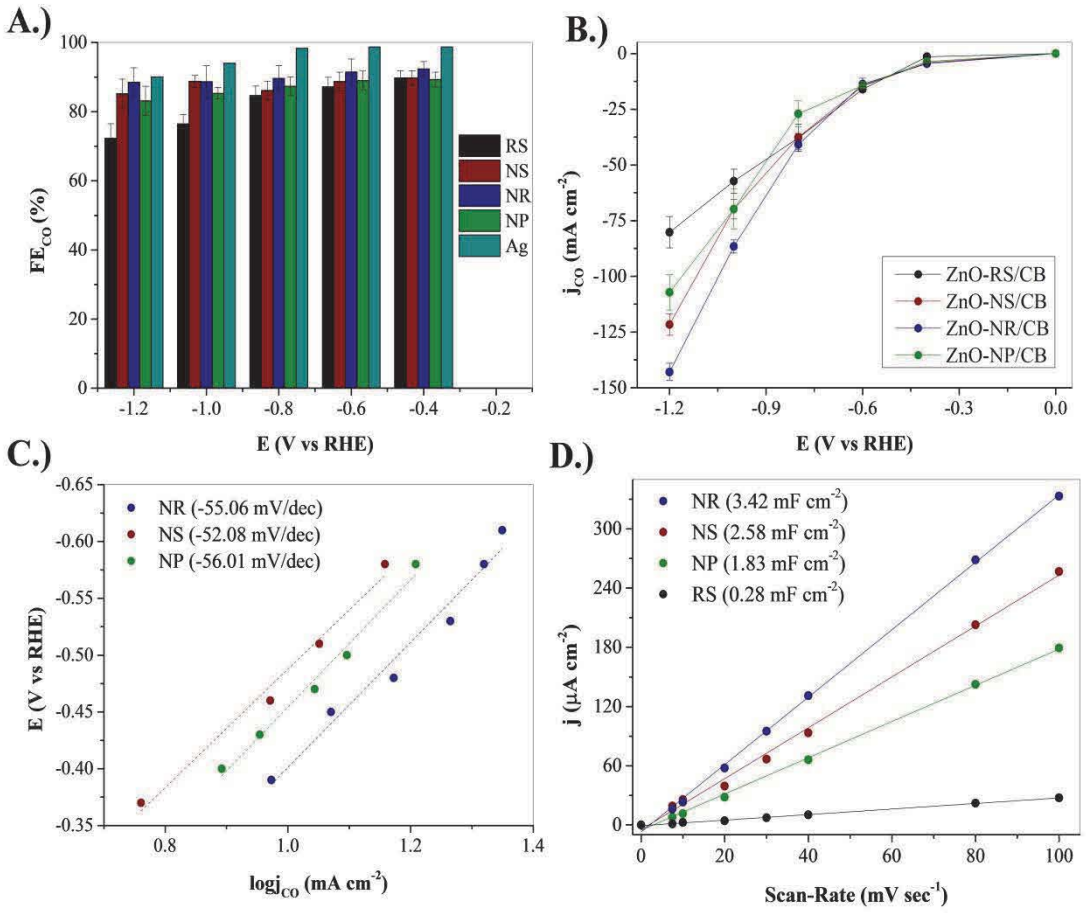

Figure 3: ECR performance of the different ZnO-based GDEs in flow-cell and electrochemical characterisation. A.) Selectivity of the GDEs towards CO (FE_{CO}) in the potential window operated in the flow-cell, B.) Partial current density (j_{CO}) of the catalyst loaded GDEs in the flow-cell, C.) Tafel-Slopes of the catalyst loaded GDEs, measured in the flow-cell set-up, D.) The C_{dl} of the different catalyst loaded GDEs, measured in H-cell using 0.1 M $NaClO_4$ (Ar saturated).

ECR performance in MEA cell configuration

MEA electrolyzers have proven to be a promising platform for ECR technology because they reduce ohmic losses and provide high energy efficiency. The cell architecture enables realistic operating conditions that are closer to a commercial application. To evaluate the performance of ZnO allotropes in the MEA cell configuration, we constructed the MEA from ZnO GDEs, an ion exchange membrane and an IrOx/Ti felt as anode. The FE_{CO} was measured in a wide current density range of 30-200 mA cm^{-2} of the three allotropes that exhibited the best performance (NP, NS, and NR) in the flow cell configuration. Figure 4 summarises the product distribution and performance of each catalyst as recorded in the MEA configuration. All three ZnO-based catalysts exhibited FE_{CO} above 80% in the current density range of 30-150 mA cm^{-2} (Figure 4 A-C). At higher current densities, an increase in FE for hydrogen was

observed on NS and NP (Figure 4A and 4C), while NR exhibits FEs for H_2 below 20% (Figure 4B). As a result, ZnO NR maintains FE_{CO} above 80% at all tested current densities. The polarisation curves of the catalysts (Figure 4D) indicate that the ZnO NR also exhibits the lowest cell voltages at all current densities, further confirming its highest catalytic activity among the allotropes (Figure 4D). Due to its higher FE_{CO} and lower cell voltage, ZnO NR shows the highest CO energy conversion (Figure S7). It should be noted that ZnO NR also outperforms Ag NPs in terms of J_{CO} and CO energy efficiency in MEA cell configuration (Figure S7 and S8). Zn-based catalysts have rarely been used in a MEA system. Nevertheless, this material shows comparable performance to those of single-atom catalysts (SACs) as non-noble- metal alternatives. [52,53]

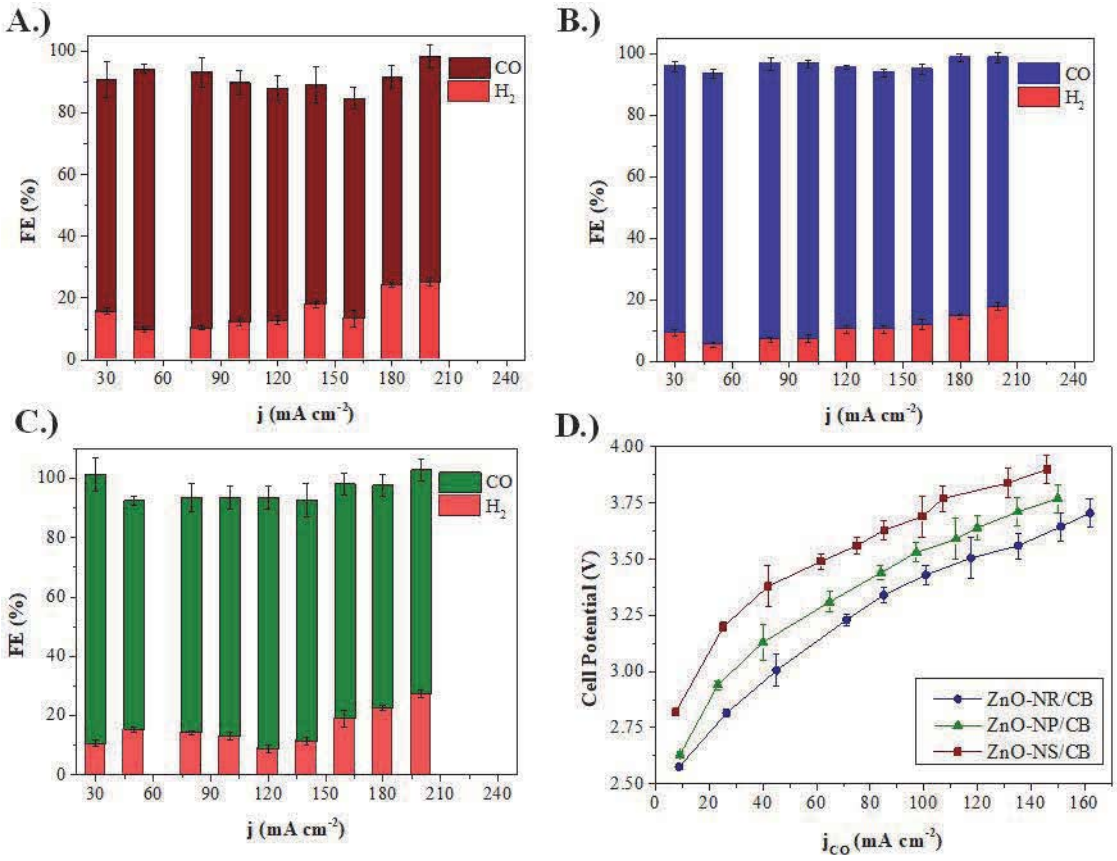

Figure 4: ECR performance of the ZnO-based GDEs in the MEA system. A.) Selectivity (FE_{CO}) of the ZnO-NS GDE, B.) Selectivity (FE_{CO}) of the ZnO-NR GDE, C.) Selectivity (FE_{CO}) of the ZnO-NP GDE, D.) Polarization curves, in terms of partial current density towards CO (j_{CO}), for the different catalyst loaded GDEs.

To investigate the stability of the catalysts in the MEA cell configuration, we applied a constant current density of -160 mA cm^{-2} and measured the change in FE_{CO} and cell voltage over time (Figure S8 and S9). As can be seen in Figure 5A, both NS and NP decrease by 50% of their initial FE_{CO} value after 10 hours of continuous reaction. In contrast, ZnO NR maintains its high CO of over 80% for the first 10 hours before

dropping to 40% after 20 hours of reaction. We performed stability test at different current densities and found that the catalysts are more stable at lower current densities (Figure 5B). This result suggests that high operating current density (i.e., high cell potential) induces physical and chemical changes in ZnO catalysts that lead to a decrease in CO selectivity. High cathodic overpotential is known to cause drastic depletion of ZnO, inducing its conversion into metallic Zn.[28] In addition, the overpotential is also related to the change in the properties of the carbon black NPs in the catalyst layer of the GDE (change in surface properties [54] and loss of hydrophobicity [55,56]). The degradation could also be associated with these changes occurring to the carbon paper properties. Previous studies have demonstrated that under ECR conditions, the GDE's hydrophobicity is seriously decreased and the electrolyte can penetrate through GDE and decreases the CO_2 diffusion, leading to the reduction in CO selectivity. [57,58]

As discussed in the flow cell section, the ZnO catalysts undergo significant changes in morphology and oxidation state during ECR, due to the reduction of ZnO to metallic Zn, which induces the change in the morphology, including aggregation (Figure S6). The same phenomenon can be observed in the MEA system. The ZnO- NR GDE exhibited the longest inherent stability for continuous ECR operation (Figure 5A). We performed SEM characterizations (Figure 5C&D) to investigate how the morphology of ZnO- NR changes under the cathodic overpotential of ECR. The first morphological changes can be observed after 2 hours of operation (Figure 5C). The catalyst exhibits a structure similar to the original structure (Figure 1D). The longer operation time leads to further changes in morphology. Figure 5D shows the morphology of the catalyst layer after 10 hours of ECR, where the threshold of stability deterioration is recorded (Figure 5A). The catalyst layer exhibits a drastic change in its morphology and adopts a layered structure with uniform distribution. We reason that the high crystallinity and high ECSA of the ZnO-NR GDE are the main reasons for its high ECR stability, because these two factors could help slow down ZnO reduction and aggregation process. To prove that high ECSA is critical to ECR stability, we increased the catalyst loading of NR to 3 mg cm^{-2} and studied its stability at 160 mA cm^{-2} current density. Indeed, the GDE maintains FE_{CO} over 80% for 50 h – a five-fold improvement compared to GDE with 1 mg cm^{-2} loading (Figure 5E).

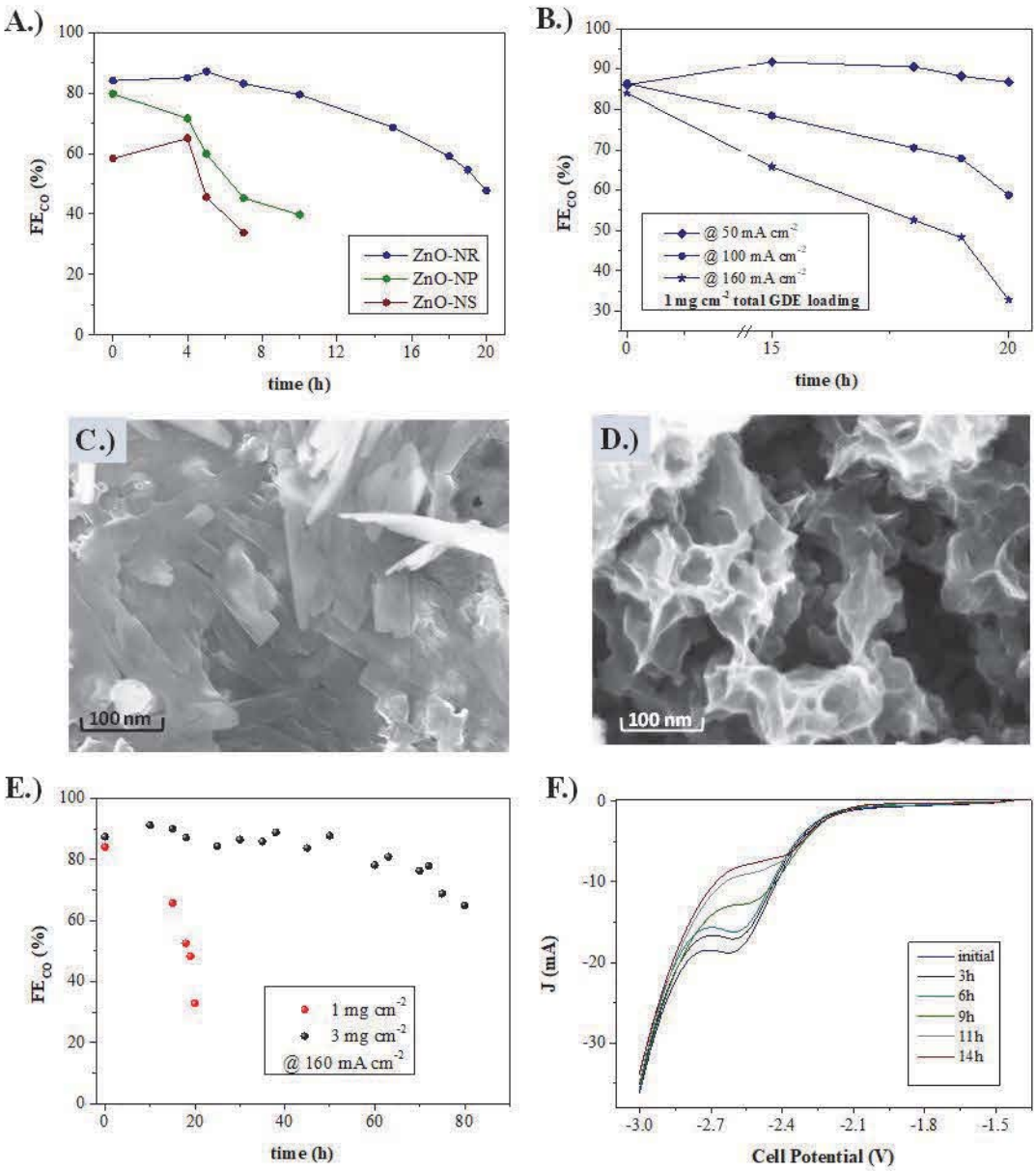

Figure 5: Stability and characteristics of the different ZnO-based GDEs in the MEA system. A.) Effect of the different morphology at the GDE stability at -160 mA cm^{-2}, B.) Effect of applying different current density at the ZnO-NR GDE, C.) & D.) SEM images of the ZnO-NR GDE after 2 h and 10 h of continuous ECR respectively, at -160 mA cm^{-2}, E.) Stability of the ZnO-NR GDE at different catalyst loading, F.) Forward CV scans during continuous operation at -160 mA cm^{-2} of the ZnO-NR GDE, tracking the ZnO shoulder.

To better understand the changes occurring on the catalyst layer, in the MEA, we acquired the Cyclic-Voltammetries (CVs) of ZnO-NR GDE during the ECR in the MEA cell. The survey CV of the MEA detects the presence of ZnO, locating a shoulder peak at a voltage of 2.5 V (Figure 5F and S10), which corresponds to the reduction of the ZnO. [59,60] The initial CV and the CV after 3 hours of operation (when the catalyst is still selectivity to CO) exhibit this distinct shoulder, owning to the presence of ZnO.

Throughout continuous operation, the ZnO-reduction shoulder exhibits a constant decrease in its intensity. While this shoulder disappeared after 14 hours of reaction (Figure 5F). This result underlines that the reduction of ZnO phase does not only co-exists with the ECR [61,62] but also that the ECR activity is closely related with the existence of the ZnO phase. [25,33, 63]

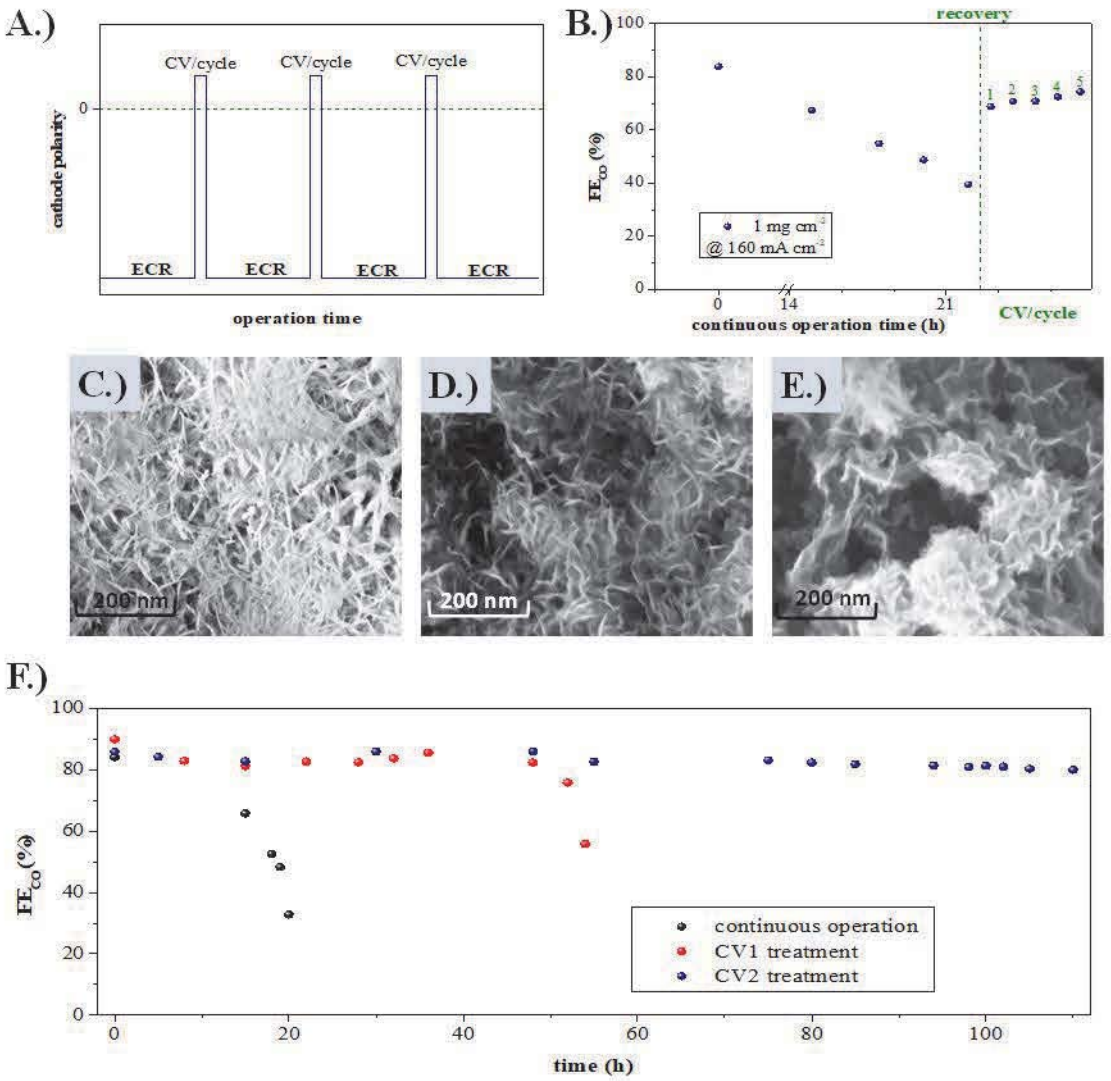

Figure 6: Stability and characteristics of the ZnO-NR by applying periodical *in-situ* electro-oxidation, during the ECR at -160 mA cm^{-2}, in the MEA system: A.) Schematic representation of the MEA operation strategy, B.) Recovery of the ZnO-NR GDE performance, by applying oxidation-CV cycles, after FE deterioration caused by continuous ECR operation, C.-E.) SEM images of the ZnO-NR GDE during our *in-situ* oxidation strategy in the MEA system (5 h, 40 h and 100 h respectively) F.) Long-term stability of the ZnO-NR GDE by applying our periodical CV oxidation strategy at different potential windows (CV treatment).

Inspired by the finding of the connection between the ZnO phase and GDE stability for ECR discussed above (Figure 5B and 5F), we hypothesize that the ECR operation time can be extended if the ZnO phase can be maintained in the GDE. While increasing the

loading of catalyst can improve the catalyst stability (Figure 5E), the FE for CO would decrease eventually because ZnO is inevitably reduced during the ECR process, as we demonstrated for the 3 mg cm^{-2} loading sample. We sought to maintain the ZnO phase during ECR, by employing an *in-situ* oxidation strategy in which the catalysts are periodically oxidized electrochemically (strategy illustrated in Figure 6A). This strategy was demonstrated previously on Cu catalysts for ECR to ethylene in a flow cell reactor.[63,64] To test this concept, we first run ECR continuously at -160 mA cm^{-2} until the FE decreased from 83% to 40% (Figure 6B). Next, we performed two CVs in the potential range of -2 to 0.5 V (Figure S10), in order to attempt to reconstruct the ZnO phase and recover the FE_{CO}. The potential window was chosen in order to ensure the oxidation of the formed metallic Zn (ZnO phase formation) [60,65], while avoiding negative potentials that would favour the ECR. After the two CVs (CV/cycle), we run the reaction for 20 min at the same current density (160 mA cm^{-2}) and found that the FE_{CO} was recovered, increasing from 40% to 65%. The FE_{CO} was further improved by repeating the CVs step, reaching 78% after 5 repeating cycles (each cycle consists of 2 CVs and 20 min of reaction at -160 mA cm^{-2}).

Having discovered that FE_{CO} can be recovered with *in-situ* oxidation CVs, we sought to establish operational protocols that involve one oxidating CV cycle followed by 1 h of continuous operation at -160 mA cm^{-2}. The CV potential window was adjusted to extend the operational time. When the oxidation window is -2 to 0.5 (CV1), FE_{CO} can be maintained for over 40 h. Further increase the potential window to -2 and 1 V (CV2) to increase oxidation current (Figure S11), the FE_{CO} was stable at over 80% for at least 100 h- an order of magnitude longer than that of continuous operation without *in-situ* oxidation step (Figure 6F). The SEM characterizations of the ZnO-NR GDE (Figure 6C-E) reveal the structural changes on the catalyst layer, during *in-situ* oxidation strategy. The ZnO-NR GDE can maintain its nanorod structure for the first few hours of reaction (Figure 6C) with in-situ regeneration strategy. For longer reaction time, a uniform nano-layered structure is formed (Figure 6D and E). Our *in-situ* approach has a direct impact on the catalyst structure, promoting a uniform distribution of the active Zn/ZnO phase and high surface area. Our strategy enables our system to exhibit stability for more than 100 h. Our results show that stable ECR can be achieved by balancing the oxidation and reduction conditions. The latest is associated with preserving both the existence and a high surface area, of the ECR-active Zn/ZnO interface. The oxidation step recovers the ZnO phase, which is present for more than 100 hours, during the long-term ECR reaction, by applying the periodical oxidation strategy (Figure S5 and S11).

Conclusions

We studied the catalytic performance of ZnO catalysts, synthesized by employing facile wet-chemical techniques in ECR using both flow cell and MEA reactors. ZnO catalysts with different morphologies show relatively high FE_{CO} of over 80% at current densities below 150 mA cm^{-2}. Among the allotropes studied, ZnO NR shows the highest FE_{CO} (over 80%) in both flow and MEA cells at a high current density range of 150-200 mA cm^{-2}. ZnO NR also shows the highest stability, maintaining a FE_{CO} over 80% for 10 hours at a current density of -160 mA cm^{-2}. We observed that the FE_{CO} of the ZnO

catalyst slowly decreased overtime due to the depletion of the ZnO oxide phase. For the first time, we have demonstrated the performance of Zn-based material in MEA and we also developed an *in-situ* regeneration strategy to maintain the oxide phase and extend the lifetime of ZnO catalysts. We demonstrated a stable FE_{CO} over 80% for 100 hours at -160 mA cm^{-2} in the MEA cell configuration. This work demonstrates the potential for practical application of inexpensive ZnO-based catalysts for large-scale ECR.

Associated Content

Supporting Information

The Supporting Information is available free of charge at https:// pubs.acs.org/

Additional SEM images of all the ZnO-based catalyst materials; XPS high-resolution spectra of O1s2; PEIS of the catalyst loaded GDEs at ECR conditions; Contact angle of the as prepared GDEs with the different morphologies; XRD patterns of the ZnO-NR GDE after different ECR operation conditions; Energy Efficiency for CO production (EE_{CO}) comparison of the ZnO-NR GDE and the Ag-GDE; Performance comparison of the ZnO-NR GDE and the Ag-GDE; Comparison of this work and the state-of-the-art materials and systems towards the CO production; Cell voltage throughout operation under CV2-treatment; Cyclic-Voltammetry profile for the ZnO-NR and Ag-NP GDEs in the MEA system; Post-mortem Cyclic-Voltammetry of the ZnO-NR by applying the oxidation strategy during long term ECR compared to the initial Cyclic-Voltammetry of the ZnO-NR GDE; Additional SEM images of the as prepared catalyst loaded GDEs; Cyclic-Voltammetry for the assessment of the C_{dl} for each of the catalyst loaded GDE.

Author Information

Corresponding Authors

Meital Shviro - Forschungszentrum Jülich GmbH, Institute of Energy and Climate Research, Electrochemical Process Engineering (IEK-14), 52425 Jülich, Germany; Chemistry and Nanoscience Center, National Renewable Energy Laboratory (NREL), Golden, CO, 80401, United States; meital.shviro@nrel.gov;

Cao-Thang Dinh - Department of Chemical Engineering, Queen's University, Kingston, Ontario, K7L 3N6, Canada; caothang.dinh@queensu.ca

Authors

Ilias Stamatelos - Forschungszentrum Jülich GmbH, Institute of Energy and Climate Research, Electrochemical Process Engineering (IEK-14), 52425 Jülich, Germany; Faculty of Mechanical Engineering, RWTH Aachen University, 52056 Aachen, Germany

Werner Lehnert - Forschungszentrum Jülich GmbH, Institute of Energy and Climate Research, Electrochemical Process Engineering (IEK-14), 52425 Jülich, Germany; Faculty of Mechanical Engineering, RWTH Aachen University, 52056 Aachen, Germany

Notes

The authors declare no competing financial interest.

Acknowledgments

The authors would like to thank Dr. Osmando F Lopes for useful and fruitful discussions. We also thank the Mitacs-Globalink award (FR77206, IT25555), that funded the collaboration of the authors for this work. C.T.D acknowledges the financial support from the Natural Sciences and Engineering Research Council of Canada (NSERC) and Queen's University.

References

(1) Kondratenko, E. V.; Mul, G.; Baltrusaitis, J.; Larrazábal, G. O.; Pérez-Ramírez, J. Status and Perspectives of CO2 Conversion into Fuels and Chemicals by Catalytic, Photocatalytic and Electrocatalytic Processes. *Energy Environ. Sci.* **2013**, *6* (11), 3112–3135. https://doi.org/10.1039/C3EE41272E.

(2) Chen, A.; Lin, B.-L. A Simple Framework for Quantifying Electrochemical CO2 Fixation. *Joule* **2018**, *2* (4), 594–606. https://doi.org/10.1016/j.joule.2018.02.003.

(3) Bushuyev, O. S.; De Luna, P.; Dinh, C. T.; Tao, L.; Saur, G.; van de Lagemaat, J.; Kelley, S. O.; Sargent, E. H. What Should We Make with CO2 and How Can We Make It? *Joule* **2018**, *2* (5), 825–832. https://doi.org/10.1016/j.joule.2017.09.003.

(4) Nitopi, S.; Bertheussen, E.; Scott, S. B.; Liu, X.; Engstfeld, A. K.; Horch, S.; Seger, B.; Stephens, I. E. L.; Chan, K.; Hahn, C.; Nørskov, J. K.; Jaramillo, T. F.; Chorkendorff, I. Progress and Perspectives of Electrochemical CO2 Reduction on Copper in Aqueous Electrolyte. *Chem. Rev.* **2019**, *119* (12), 7610–7672. https://doi.org/10.1021/acs.chemrev.8b00705.

(5) Liu, X.; Xiao, J.; Peng, H.; Hong, X.; Chan, K.; Nørskov, J. K. Understanding Trends in Electrochemical Carbon Dioxide Reduction Rates. *Nat. Commun.* **2017**, *8* (1), 15438. https://doi.org/10.1038/ncomms15438.

(6) Rosen, J.; Hutchings, G. S.; Lu, Q.; Rivera, S.; Zhou, Y.; Vlachos, D. G.; Jiao, F. Mechanistic Insights into the Electrochemical Reduction of CO2 to CO on Nanostructured Ag Surfaces. *ACS Catal.* **2015**, *5* (7), 4293–4299. https://doi.org/10.1021/acscatal.5b00840.

(7) Liang, F.; Zhang, K.; Zhang, L.; Zhang, Y.; Lei, Y.; Sun, X. Recent Development of Electrocatalytic CO2 Reduction Application to Energy Conversion. *Small* **2021**, *17* (44), 2100323. https://doi.org/10.1002/smll.202100323.

(8) Burdyny, T.; Smith, W. A. CO2 Reduction on Gas-Diffusion Electrodes and Why Catalytic Performance Must Be Assessed at Commercially-Relevant Conditions. *Energy Environ. Sci.* **2019**, *12* (5), 1442–1453. https://doi.org/10.1039/C8EE03134G.

(9) Garg, S.; Li, M.; Weber, A. Z.; Ge, L.; Li, L.; Rudolph, V.; Wang, G.; Rufford, T. E. Advances and Challenges in Electrochemical CO2 Reduction Processes: An Engineering

and Design Perspective Looking beyond New Catalyst Materials. *J. Mater. Chem. A* **2020**, *8* (4), 1511–1544. https://doi.org/10.1039/C9TA13298H.

(10) Jouny, M.; Luc, W.; Jiao, F. General Techno-Economic Analysis of CO2 Electrolysis Systems. *Ind. Eng. Chem. Res.* **2018**, *57* (6), 2165–2177. https://doi.org/10.1021/acs.iecr.7b03514.

(11) Spurgeon, J. M.; Kumar, B. A Comparative Technoeconomic Analysis of Pathways for Commercial Electrochemical CO2 Reduction to Liquid Products. *Energy Environ. Sci.* **2018**, *11* (6), 1536–1551. https://doi.org/10.1039/C8EE00097B.

(12) Martín, A. J.; Larrazábal, G. O.; Pérez-Ramírez, J. Towards Sustainable Fuels and Chemicals through the Electrochemical Reduction of CO2: Lessons from Water Electrolysis. *Green Chem.* **2015**, *17* (12), 5114–5130. https://doi.org/10.1039/C5GC01893E.

(13) Spurgeon, J. M.; Kumar, B. A Comparative Technoeconomic Analysis of Pathways for Commercial Electrochemical CO2 Reduction to Liquid Products. *Energy Environ. Sci.* **2018**, *11* (6), 1536–1551. https://doi.org/10.1039/C8EE00097B.

(14) Kortlever, R.; Shen, J.; Schouten, K. J. P.; Calle-Vallejo, F.; Koper, M. T. M. *Catalysts and Reaction Pathways for the Electrochemical Reduction of Carbon Dioxide*. ACS Publications. https://pubs.acs.org/doi/pdf/10.1021/acs.jpclett.5b01559 (accessed 2021-11-17). https://doi.org/10.1021/acs.jpclett.5b01559.

(15) Feaster, J. T.; Shi, C.; Cave, E. R.; Hatsukade, T.; Abram, D. N.; Kuhl, K. P.; Hahn, C.; Nørskov, J. K.; Jaramillo, T. F. Understanding Selectivity for the Electrochemical Reduction of Carbon Dioxide to Formic Acid and Carbon Monoxide on Metal Electrodes. *ACS Catal.* **2017**, *7* (7), 4822–4827. https://doi.org/10.1021/acscatal.7b00687.

(16) Larrazábal, G. O.; Martín, A. J.; Pérez-Ramírez, J. Building Blocks for High Performance in Electrocatalytic CO2 Reduction: Materials, Optimization Strategies, and Device Engineering. *J. Phys. Chem. Lett.* **2017**, *8* (16), 3933–3944. https://doi.org/10.1021/acs.jpclett.7b01380.

(17) Verma, S.; Kim, B.; Jhong, H.-R. "Molly"; Ma, S.; Kenis, P. J. A. A Gross-Margin Model for Defining Technoeconomic Benchmarks in the Electroreduction of CO2. *ChemSusChem* **2016**, *9* (15), 1972–1979. https://doi.org/10.1002/cssc.201600394.

(18) M. Spurgeon, J.; Kumar, B. A Comparative Technoeconomic Analysis of Pathways for Commercial Electrochemical CO 2 Reduction to Liquid Products. *Energy Environ. Sci.* **2018**, *11* (6), 1536–1551. https://doi.org/10.1039/C8EE00097B.

(19) Guo, R.-H.; Liu, C.-F.; Wei, T.-C.; Hu, C.-C. Electrochemical Behavior of CO2 Reduction on Palladium Nanoparticles: Dependence of Adsorbed CO on Electrode Potential. *Electrochem. Commun.* **2017**, *80*, 24–28. https://doi.org/10.1016/j.elecom.2017.05.005.

(20) Dinh, C.-T.; García de Arquer, F. P.; Sinton, D.; Sargent, E. H. High Rate, Selective, and Stable Electroreduction of CO2 to CO in Basic and Neutral Media. *ACS Energy Lett.* **2018**, *3* (11), 2835–2840. https://doi.org/10.1021/acsenergylett.8b01734.

(21) Chen, Y.; Li, C. W.; Kanan, M. W. Aqueous CO2 Reduction at Very Low Overpotential on Oxide-Derived Au Nanoparticles. *J. Am. Chem. Soc.* **2012**, *134* (49), 19969–19972. https://doi.org/10.1021/ja309317u.

(22) Rosen, J.; Hutchings, G. S.; Lu, Q.; Forest, R. V.; Moore, A.; Jiao, F. Electrodeposited Zn Dendrites with Enhanced CO Selectivity for Electrocatalytic CO2 Reduction. *ACS Catal.* **2015**, *5* (8), 4586–4591. https://doi.org/10.1021/acscatal.5b00922.

(23) Zhang, T.; Li, X.; Qiu, Y.; Su, P.; Xu, W.; Zhong, H.; Zhang, H. Multilayered Zn Nanosheets as an Electrocatalyst for Efficient Electrochemical Reduction of CO2. *J. Catal.* **2018**, *357*, 154–162. https://doi.org/10.1016/j.jcat.2017.11.003.

(24) Won, D. H.; Shin, H.; Koh, J.; Chung, J.; Lee, H. S.; Kim, H.; Woo, S. I. Highly Efficient, Selective, and Stable CO2 Electroreduction on a Hexagonal Zn Catalyst. *Angew. Chem. Int. Ed.* **2016**, *55* (32), 9297–9300. https://doi.org/10.1002/anie.201602888.

(25) Nguyen, D. L. T.; Jee, M. S.; Won, D. H.; Jung, H.; Oh, H.-S.; Min, B. K.; Hwang, Y. J. Selective CO2 Reduction on Zinc Electrocatalyst: The Effect of Zinc Oxidation State Induced by Pretreatment Environment. *ACS Sustain. Chem. Eng.* **2017**, *5* (12), 11377–11386. https://doi.org/10.1021/acssuschemeng.7b02460.

(26) Lamaison, S.; Wakerley, D.; Kracke, F.; Moore, T.; Zhou, L.; Lee, D. U.; Wang, L.; Hubert, M. A.; Aviles Acosta, J. E.; Gregoire, J. M.; Duoss, E. B.; Baker, S.; Beck, V. A.; Spormann, A. M.; Fontecave, M.; Hahn, C.; Jaramillo, T. F. Designing a Zn–Ag Catalyst Matrix and Electrolyzer System for CO2 Conversion to CO and Beyond. *Adv. Mater.* **2022**, *34* (1), 2103963. https://doi.org/10.1002/adma.202103963.

(27) Luo, W.; Zhang, J.; Li, M.; Züttel, A. Boosting CO Production in Electrocatalytic CO2 Reduction on Highly Porous Zn Catalysts. *ACS Catal.* **2019**, *9* (5), 3783–3791. https://doi.org/10.1021/acscatal.8b05109.

(28) Jiang, X.; Cai, F.; Gao, D.; Dong, J.; Miao, S.; Wang, G.; Bao, X. Electrocatalytic Reduction of Carbon Dioxide over Reduced Nanoporous Zinc Oxide. *Electrochem. Commun.* **2016**, *68*, 67–70. https://doi.org/10.1016/j.elecom.2016.05.003.

(29) Han, K.; Ngene, P.; Jongh, P. de. Structure Dependent Product Selectivity for CO2 Electroreduction on ZnO Derived Catalysts. *ChemCatChem n/a* (n/a). https://doi.org/10.1002/cctc.202001710.

(30) Li, C.; Shen, G.; Zhang, R.; Wu, D.; Zou, C.; Ling, T.; Liu, H.; Dong, C.; Du, X.-W. Zn Nanosheets Coated with a ZnS Subnanometer Layer for Effective and Durable CO2 Reduction. *J. Mater. Chem. A* **2019**, *7* (4), 1418–1423. https://doi.org/10.1039/C8TA10799H.

(31) Xiang, Q.; Li, F.; Wang, J.; Chen, W.; Miao, Q.; Zhang, Q.; Tao, P.; Song, C.; Shang, W.; Zhu, H.; Deng, T.; Wu, J. Heterostructure of ZnO Nanosheets/Zn with a Highly Enhanced Edge Surface for Efficient CO2 Electrochemical Reduction to CO. *ACS Appl. Mater. Interfaces* **2021**, *13* (9), 10837–10844. https://doi.org/10.1021/acsami.0c20302.

(32) Effect of 3d-Transition Metals Doped in ZnO Monolayers on the CO2 Electrochemical Reduction to Valuable Products: First Principles Study. *Appl. Surf. Sci.* **2021**, *550*, 149380. https://doi.org/10.1016/j.apsusc.2021.149380.

(33) Geng, Z.; Kong, X.; Chen, W.; Su, H.; Liu, Y.; Cai, F.; Wang, G.; Zeng, J. Oxygen Vacancies in ZnO Nanosheets Enhance CO2 Electrochemical Reduction to CO. *Angew. Chem. Int. Ed.* **2018**, *57* (21), 6054–6059. https://doi.org/10.1002/anie.201711255.

(34) Liu, Y.; Liu, H.; Zhang, Q.; Li, T. Adjusting the Proportions of {0001} Facets and High-Index Facets of ZnO Hexagonal Prisms and Their Photocatalytic Activity. *RSC Adv.* **2017**, *7* (6), 3515–3520. https://doi.org/10.1039/C6RA24912D.

(35) Zong, X.; Jin, Y.; Li, Y.; Zhang, X.; Zhang, S.; Xie, H.; Zhang, J.; Xiong, Y. Morphology-Controllable ZnO Catalysts Enriched with Oxygen-Vacancies for Boosting CO2 Electroreduction to CO. *J. CO2 Util.* **2022**, *61*, 102051. https://doi.org/10.1016/j.jcou.2022.102051.

(36) Zeng, J.; Fontana, M.; Sacco, A.; Sassone, D.; Pirri, C. F. A Study of the Effect of Electrode Composition on the Electrochemical Reduction of CO2. *Catal. Today* **2021**. https://doi.org/10.1016/j.cattod.2021.07.014.

(37) Li, J.; Fan, H.; Jia, X. Multilayered ZnO Nanosheets with 3D Porous Architectures: Synthesis and Gas Sensing Application. *J. Phys. Chem. C* **2010**, *114* (35), 14684–14691. https://doi.org/10.1021/jp100792c.

(38) Li, J.; Fan, H.; Jia, X. Multilayered ZnO Nanosheets with 3D Porous Architectures: Synthesis and Gas Sensing Application. *J. Phys. Chem. C* **2010**, *114* (35), 14684–14691. https://doi.org/10.1021/jp100792c.
(39) Chubarov, M.; Choudhury, T. H.; Zhang, X.; Redwing, J. M. In-Plane x-Ray Diffraction for Characterization of Monolayer and Few-Layer Transition Metal Dichalcogenide Films. *Nanotechnology* **2018**, *29* (5), 055706. https://doi.org/10.1088/1361-6528/aaa1bd.
(40) Bera, S.; Mittal, V. K.; Venkata Krishnan, R.; Saravanan, T.; Velmurugan, S.; Nagarajan, K.; Narasimhan, S. V. XPS Analysis of UxCe1−xO2±δ and Determination of Oxygen to Metal Ratio. *J. Nucl. Mater.* **2009**, *393* (1), 120–125. https://doi.org/10.1016/j.jnucmat.2009.05.015.
(41) Kadari, A.; Schemme, T.; Kadri, D.; Wollschläger, J. XPS and Morphological Properties of Cr2O3 Thin Films Grown by Thermal Evaporation Method. *Results Phys.* **2017**, *7*, 3124–3129. https://doi.org/10.1016/j.rinp.2017.08.036.
(42) Li, P.; Liu, J.; Bi, J.; Zhu, Q.; Wu, T.; Ma, J.; Zhang, F.; Jia, J.; Han, B. Tuning the Efficiency and Product Composition for Electrocatalytic CO2 Reduction to Syngas over Zinc Films by Morphology and Wettability. *Green Chem.* **2022**. https://doi.org/10.1039/D1GC04364A.
(43) Zhang, T.; Zhong, H.; Qiu, Y.; Li, X.; Zhang, H. Zn Electrode with a Layer of Nanoparticles for Selective Electroreduction of CO2 to Formate in Aqueous Solutions. *J. Mater. Chem. A* **2016**, *4* (42), 16670–16676. https://doi.org/10.1039/C6TA07000K.
(44) Zhang, J.; Yin, R.; Shao, Q.; Zhu, T.; Huang, X. Oxygen Vacancies in Amorphous InOx Nanoribbons Enhance CO2 Adsorption and Activation for CO2 Electroreduction. *Angew. Chem. Int. Ed.* **2019**, *58* (17), 5609–5613. https://doi.org/10.1002/anie.201900167.
(45) Shinagawa, T.; Garcia-Esparza, A. T.; Takanabe, K. Insight on Tafel Slopes from a Microkinetic Analysis of Aqueous Electrocatalysis for Energy Conversion. *Sci. Rep.* **2015**, *5* (1), 13801. https://doi.org/10.1038/srep13801.
(46) Hosseini, S.; Savaloni, H.; Gholipour Shahraki, M. Influence of Surface Morphology and Nano-Structure on Hydrophobicity: A Molecular Dynamics Approach. *Appl. Surf. Sci.* **2019**, *485*, 536–546. https://doi.org/10.1016/j.apsusc.2019.04.236.
(47) Yoshimitsu, Z.; Nakajima, A.; Watanabe, T.; Hashimoto, K. Effects of Surface Structure on the Hydrophobicity and Sliding Behavior of Water Droplets. *Langmuir* **2002**, *18* (15), 5818–5822. https://doi.org/10.1021/la020088p.
(48) Xing, Z.; Hu, L.; Ripatti, D. S.; Hu, X.; Feng, X. Enhancing Carbon Dioxide Gas-Diffusion Electrolysis by Creating a Hydrophobic Catalyst Microenvironment. *Nat. Commun.* **2021**, *12* (1), 136. https://doi.org/10.1038/s41467-020-20397-5.
(49) Luo, W.; Zhang, Q.; Zhang, J.; Moioli, E.; Zhao, K.; Züttel, A. Electrochemical Reconstruction of ZnO for Selective Reduction of CO2 to CO. *Appl. Catal. B Environ.* **2020**, *273*, 119060. https://doi.org/10.1016/j.apcatb.2020.119060.
(50) Wang, J.; Zhu, Z.; Wei, X.; Li, Z.; Chen, J. S.; Wu, R.; Wei, Z. Hydrogen-Mediated Synthesis of 3D Hierarchical Porous Zinc Catalyst for CO2 Electroreduction with High Current Density. *J. Phys. Chem. C* **2021**. https://doi.org/10.1021/acs.jpcc.1c07498.
(51) Löffler, M.; Mayrhofer, K. J. J.; Katsounaros, I. Oxide Reduction Precedes Carbon Dioxide Reduction on Oxide-Derived Copper Electrodes. *J. Phys. Chem. C* **2021**, *125* (3), 1833–1838. https://doi.org/10.1021/acs.jpcc.0c09107.
(52) Jeong, H.-Y.; Balamurugan, M.; Choutipalli, V. S. K.; Jeong, E.; Subramanian, V.; Sim, U.; Nam, K. T. Achieving Highly Efficient CO2 to CO Electroreduction Exceeding 300 MA Cm−2 with Single-Atom Nickel Electrocatalysts. *J. Mater. Chem. A* **2019**, *7* (17), 10651–10661. https://doi.org/10.1039/C9TA02405K.

(53) Zheng, T.; Jiang, K.; Ta, N.; Hu, Y.; Zeng, J.; Liu, J.; Wang, H. Large-Scale and Highly Selective CO2 Electrocatalytic Reduction on Nickel Single-Atom Catalyst. *Joule* **2019**, *3* (1), 265–278. https://doi.org/10.1016/j.joule.2018.10.015.
(54) Pérez-Rodríguez, S.; Pastor, E.; Lázaro, M. J. Electrochemical Behavior of the Carbon Black Vulcan XC-72R: Influence of the Surface Chemistry. *Int. J. Hydrog. Energy* **2018**, *43* (16), 7911–7922. https://doi.org/10.1016/j.ijhydene.2018.03.040.
(55) Wang, Q.; Wang, X.; Wu, C.; Cheng, Y.; Sun, Q.; Dong, H.; Yu, H. Electrodeposition of Tin on Nafion-Bonded Carbon Black as an Active Catalyst Layer for Efficient Electroreduction of CO2 to Formic Acid. *Sci. Rep.* **2017**, *7* (1), 13711. https://doi.org/10.1038/s41598-017-14233-y.
(56) Xing, Z.; Hu, L.; Ripatti, D. S.; Hu, X.; Feng, X. Enhancing Carbon Dioxide Gas-Diffusion Electrolysis by Creating a Hydrophobic Catalyst Microenvironment. *Nat. Commun.* **2021**, *12* (1), 136. https://doi.org/10.1038/s41467-020-20397-5.
(57) Dinh, C.-T.; Burdyny, T.; Kibria, M. G.; Seifitokaldani, A.; Gabardo, C. M.; García de Arquer, F. P.; Kiani, A.; Edwards, J. P.; De Luna, P.; Bushuyev, O. S.; Zou, C.; Quintero-Bermudez, R.; Pang, Y.; Sinton, D.; Sargent, E. H. CO2 Electroreduction to Ethylene via Hydroxide-Mediated Copper Catalysis at an Abrupt Interface. *Science* **2018**, *360* (6390), 783–787. https://doi.org/10.1126/science.aas9100.
(58) Ma, W.; Xie, S.; Liu, T.; Fan, Q.; Ye, J.; Sun, F.; Jiang, Z.; Zhang, Q.; Cheng, J.; Wang, Y. Electrocatalytic Reduction of CO2 to Ethylene and Ethanol through Hydrogen-Assisted C–C Coupling over Fluorine-Modified Copper. *Nat. Catal.* **2020**, *3* (6), 478–487. https://doi.org/10.1038/s41929-020-0450-0.
(59) Maikap, A.; Mukherjee, K.; Mondal, B.; Mandal, N. Zinc Oxide Thin Film Based Nonenzymatic Electrochemical Sensor for the Detection of Trace Level Catechol. *RSC Adv.* **2016**, *6* (69), 64611–64616. https://doi.org/10.1039/C6RA09598D.
(60) Fatin, S. O.; Lim, H. N.; Tan, W. T.; Huang, N. M. Comparison of Photocatalytic Activity and Cyclic Voltammetry of Zinc Oxide and Titanium Dioxide Nanoparticles toward Degradation of Methylene Blue. *Int J Electrochem Sci* **2012**, *7*, 11.
(61) Hjorth, I.; Nord, M.; Rønning, M.; Yang, J.; Chen, D. Electrochemical Reduction of CO2 to Synthesis Gas on CNT Supported CuxZn1-x O Catalysts. *Catal. Today* **2020**, *357*, 311–321. https://doi.org/10.1016/j.cattod.2019.02.045.
(62) Löffler, M.; Mayrhofer, K. J. J.; Katsounaros, I. Oxide Reduction Precedes Carbon Dioxide Reduction on Oxide-Derived Copper Electrodes. *J. Phys. Chem. C* **2021**, *125* (3), 1833–1838. https://doi.org/10.1021/acs.jpcc.0c09107.
(63) Nguyen, T. N.; Chen, Z.; Zeraati, A. S.; Shiran, H. S.; Sadaf, S. Md.; Kibria, M. G.; Sargent, E. H.; Dinh, C.-T. Catalyst Regeneration via Chemical Oxidation Enables Long-Term Electrochemical Carbon Dioxide Reduction. *J. Am. Chem. Soc.* **2022**, *144* (29), 13254–13265. https://doi.org/10.1021/jacs.2c04081.
(64) Obasanjo, C. A.; Zeraati, A. S.; Shiran, H. S.; Nguyen, T. N.; Sadaf, S. M.; Kibria, M. G.; Dinh, C.-T. In Situ Regeneration of Copper Catalysts for Long-Term Electrochemical CO2 Reduction to Multiple Carbon Products. *J. Mater. Chem. A* **2022**. https://doi.org/10.1039/D2TA02709G.
(65) Nguyen, D. L. T.; Jee, M. S.; Won, D. H.; Jung, H.; Oh, H.-S.; Min, B. K.; Hwang, Y. J. Selective CO2 Reduction on Zinc Electrocatalyst: The Effect of Zinc Oxidation State Induced by Pretreatment Environment. *ACS Sustain. Chem. Eng.* **2017**, *5* (12), 11377–11386. https://doi.org/10.1021/acssuschemeng.7b02460.
(66) Ghorbani, H. R.; Mehr, F. P.; Pazoki, H.; Rahmani, B. M. Synthesis of ZnO Nanoparticles by Precipitation Method. *Orient. J. Chem.* **2015**, *31* (2), 1219–1221.
(67) Zhang, J.; Wang, W.; Zhu, P.; Chen, J.; Zhang, Z.; Wu, Z. Synthesis of Small Diameter ZnO Nanorods via Refluxing Route in Alcohol–Water Mixing Solution Containing Zinc

Salt and Urea. *Mater. Lett.* **2007**, *61* (2), 592–594. https://doi.org/10.1016/j.matlet.2006.05.018.

(68) Yang, F. Size Effect on Electric-Double-Layer Capacitances of Conducting Structures. *Phys. Lett. A* **2019**, *383* (20), 2353–2360. https://doi.org/10.1016/j.physleta.2019.04.051.

TOC

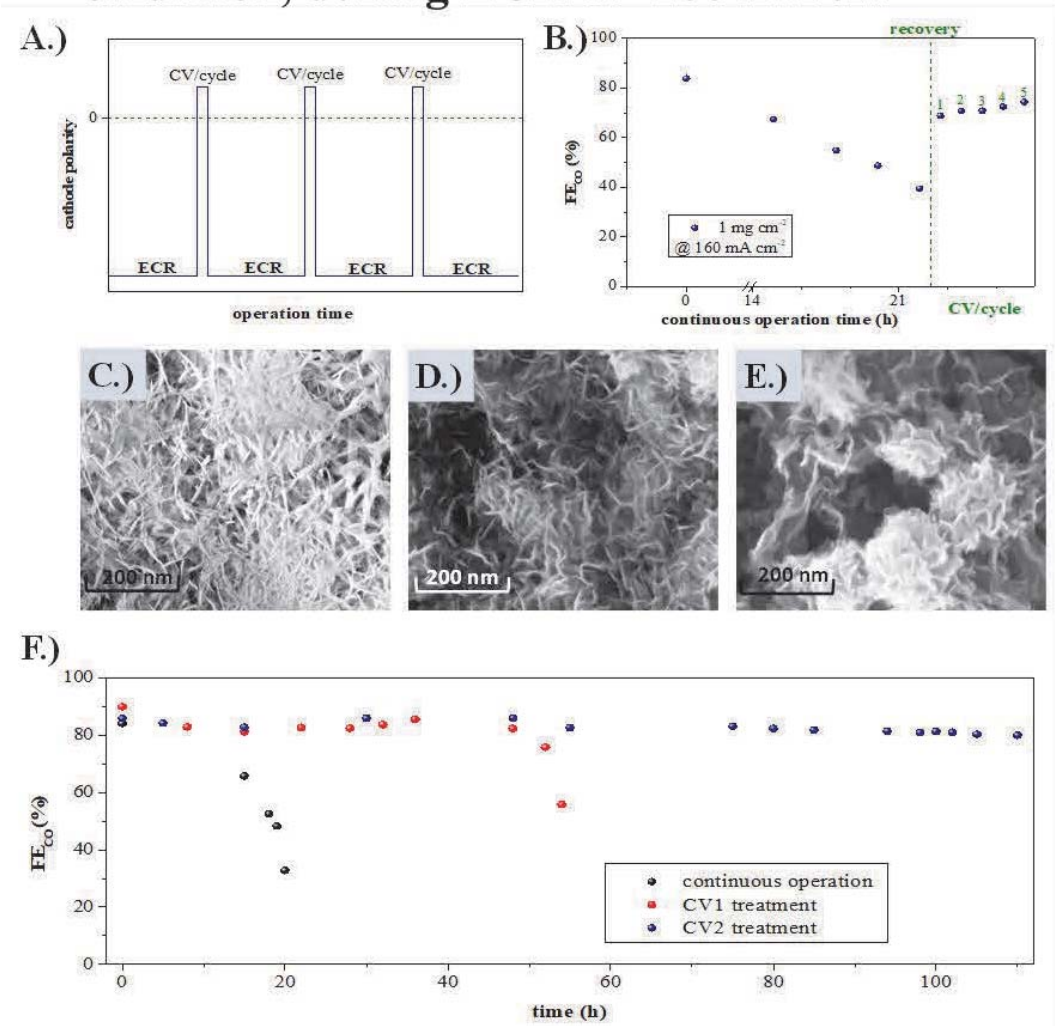
Stability and characteristics of ZnO-Nanorods by applying periodical *in-situ* electro-oxidation, during ECR at -160 mA cm-2
A.)
CV/cycle
CV/cycle
CV/cycle
0
cathode polarity
ECR
ECR
ECR
ECR
operation time
B.)
recovery
100
80
60
40
20
0
FE_CO (%)
1 mg cm-2
@ 160 mA cm-2
1
2
3
4
5
0
14
21
continuous operation time (h)
CV/cycle
C.)
200 nm
D.)
200 nm
E.)
200 nm
F.)
100
80
60
40
20
0
FE_CO (%)
continuous operation
CV1 treatment
CV2 treatment
0
20
40
60
80
100
time (h)